Predicting Angular Displacement of Medical Devices in a MRI Scanner Bore Using COMSOL Multiphysics

A Thesis

Submitted to the Faculty

of

Drexel University

by

Adam Ferreira

in partial fulfillment of the

requirements for the degree

of

Master of Science in Biomedical Engineering

April 2017

Table of Contents

List of Tables

List of Figures

Abstract

Predicting Angular Displacement of Medical Devices in a MRI Scanner Bore Using COMSOL Multiphysics

Adam Ferreira

Medical devices undergo a series of evaluations in order to determine their performance and level of safety in a magnetic resonance (MR) environment. The standard of focus for this work is ASTM F2052-15 which measures the induced displacement of a device due to the spatial gradient fields present in the MRI scanner bore. This test entails suspending the device from a string near the entrance of the MRI bore and measuring the angle of deflection.

Evaluating the performance of medical devices in the MR environment is a costly endeavor, both in time and resources. This work aims to develop a predictive model to help eliminate some of the burden associated with this testing. The current method of testing magnetically induced displacement force is by measuring the deflection angle between the device and the test fixture. The displacement force is then computed using this deflection angle. It is expected that this deflection angle can be recreated within the simulation and the forces acting on the device be accurately displayed, and the associated displacement force estimated numerically.

This model provides the freedom of manipulating a device and evaluating its performance almost instantaneously. Extensions of this model have the potential to further the detailed numerical evaluation of medical devices in the MR environment. This information could lead to reevaluation of the current ASTM standards surrounding medical devices in the MR environment.

1. Introduction

1.1. Problem Statement

The introduction of magnetic resonance imaging (MRI) to the clinical setting proved to be a monumental improvement to the world of diagnostic medicine. MRI scanners utilize a series of magnets and coils to produce high-quality two dimensional images of human tissues. Utilizing different frequencies, scan parameters, and contrast materials clinicians can target specific area and tissue types in search of irregularities and diseases. The magnetic field and radiofrequencies utilized do not have any damaging effects on biological tissues [1]. However, as with any medical procedure, there are a number of risks associated with magnetic resonance imaging.

While the tools utilized during a MRI scan are not associated with any direct negative consequences in biological tissues, there are other devices that may be present in the body that could create potential safety concerns. Due to the technological advances in the medical device industry, an increasing number of people have some form of implanted device such as orthopedic implants, vascular stents, pacemakers, etc. These devices are composed of materials whose magnetic properties vastly differ from biological tissues. The material properties of certain devices cause unwanted interactions with the magnetic field, opening the door to a number of negative consequences, including but not limited to image artifacts, RF induced heating, translational forces, and torque.

The most concerning of the potential risks associated with imaging patients with implanted devices is the potential for a device to experience translational forces or torques. MRI scanners are extremely powerful magnets that create a static magnetic field

in and around the scanner bore. This magnetic field has a tendency to attract items composed of ferromagnetic material into the center of its bore. Due to the invisible nature of the magnetic field, its presence is often neglected or forgotten creating the potential for a catastrophic incident. The strength of the magnetic field does not linearly increase as you approach the bore, which means that the force of attraction on a ferromagnetic object can suddenly increase to a dangerous level. Figure 1 details the result of a hospital bed containing ferromagnetic material getting too close the MRI scanner bore.

Figure 1: Result of a MRI-unsafe hospital bed getting too close to a MRI scanner [2].

In 1997 the FDA determined that there should be a series of standards that outlined the requirements for medical devices to be considered “MRI safe”. The FDA enlisted the American Society for Testing and Materials to develop guidelines for evaluating the safety and efficiency of medical devices in MR environments [3]. Since those initially formed guidelines, ASTM has created a series of standards that define the methods for testing and analyzing medical devices with the goal of continuous improvement. ASTM 2052-15, a standard which highlights an experimental procedure for measuring translational forces on medical devices, will be the main focus of this paper [4].

1.2. Aim 1

The magnetic fields created by an MRI scanner bore vary between devices, even between those of the same make and model. In order to create an effective predictive application, the static magnetic fields present in the magnetic resonance environment must be accurately characterized. The first aim of this Master’s Thesis is to develop a repeatable and efficient procedure for mapping the spatial gradients within the MRI bore. This includes creating a fixture and test method that can be implemented on a number of MRI scanners.

1.3. Aim 2

The second objective of this thesis is to create a predictive application capable of assessing angular displacement of medical devices in a MRI scanner bore. This application models the experimental procedure described in ASTM 2052-15, “Standard Test Method for Measurement of Magnetically Induced Displacement Force in the

Magnetic Resonance Environment". This model should be able to predict angular deflections values within three degrees of experimentally measured data.

2. Aim 1

2.1. Background

2.1.1. Coordinate System

It is important to clarify the orientation of the coordinate system used in MRI applications as it differs slightly from the conventional system. The front face of the scanner bore is in the XY plane with center axis of the bore aligned with the Z axis. A schematic of the coordinate system is shown in Figure 2 below.

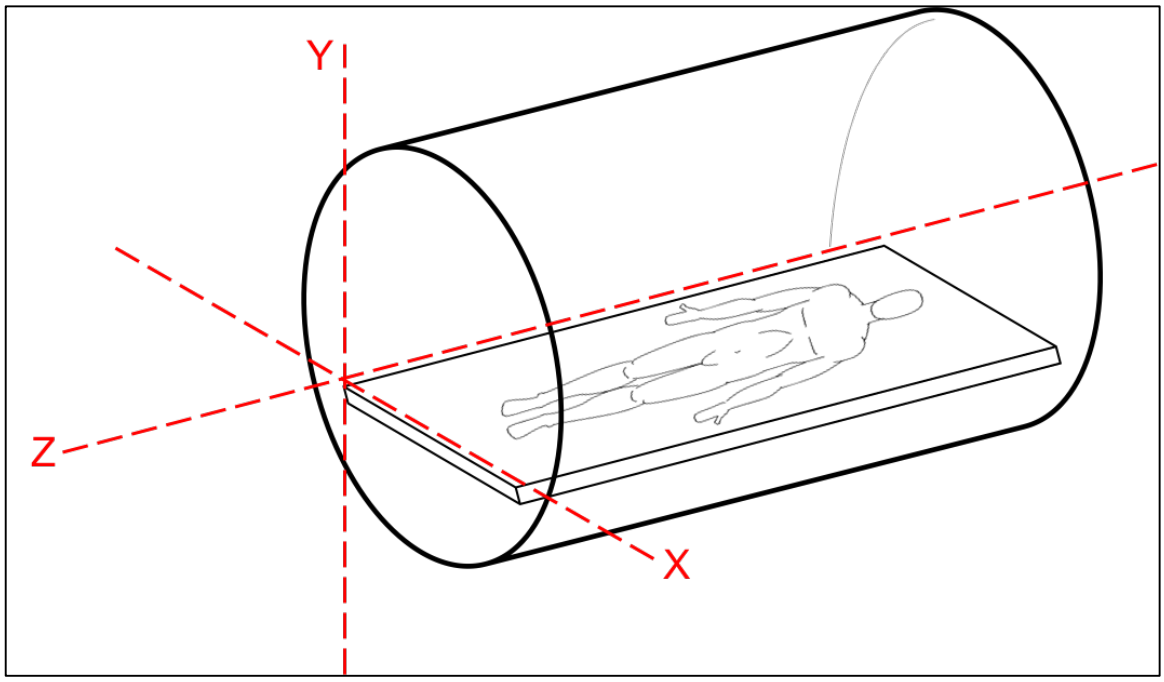

Figure 2: This schematic shows a rough outline of a scanner bore with a patient on the scanner table inside. The coordinate system is indicated in red.

The coordinate system is oriented with the positive Z direction exiting the scanner opening. This coordinate system will be referenced in this orientation throughout the rest of this paper.

2.1.2. Magnetic Resonance Imaging

Nuclear magnetic resonance (NMR) imaging was developed in the early 1980's as a safer technique for imaging biological tissues. NMR imaging, commonly referred to as magnetic resonance imaging (MRI), relies on the magnetic fields produced by protons found in the nuclei of hydrogen atoms which are present in excess within the body through water and fat cells. MRI machines are comprised of a series of magnets and coils that create a static magnetic field within and surrounding the scanner bore. Technicians apply specific radio frequencies (RF) that align the protons present in the tissues of the body with the magnetic fields present in the MRI scanner. However, the imaging procedures and field manipulation techniques used in clinical MRI settings is beyond the scope of this thesis. Instead, the emphasis will be focused on the equipment responsible for producing the static magnetic fields.

The main component of a MRI scanner is the magnet that creates the static magnetic field present in and around the bore. The majority of MRI systems utilize superconducting magnets to generate this magnetic field because of their potential field strength and homogeneity. Superconducting magnets create a magnetic field by passing a current through a coil composed of superconductor material, typically Niobium-Titanium. The magnetic field is maintained provided a current is flowing through the coil. Superconductors are used in this application due to their resistive properties in extremely low temperatures. Below 9.5° K Niobium-Titanium coils experience no electrical resistance so the current in the coils doesn't degrade and the magnetic field remains intact (provided that the coils are kept at the correct temperature) [5].

The static magnetic field that is created through the superconductor magnet can be visualized as a series of field lines that run through the bore in the negative Z direction before looping up and back around (see Figure 3). The magnetic flux density, measured in Tesla, is greatest at the isocenter of the bore (labeled A in Figure 3) and also indicates where the magnetic field is homogeneous. The greatest change in magnetic field per unit of distance is known as the spatial gradient of the magnetic field. For example, dB/dz is the spatial gradient of the magnetic field in the Z direction. The spatial gradient of the magnetic field is greatest near the entrance of the bore as the field strength drastically decreases at that point.

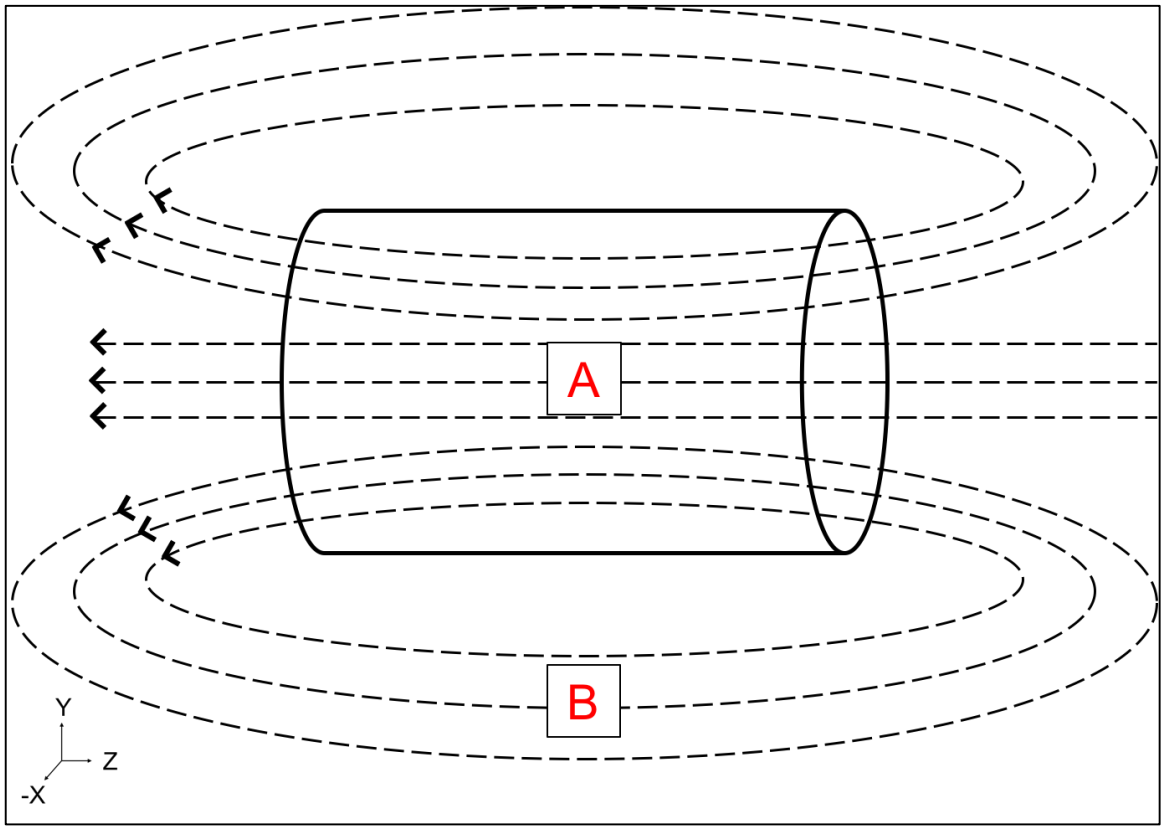

Figure 3: Diagram adapted from Shellock et al [2]. Magnetic field lines created by MRI superconductor coil. Isocenter indicated with red 'A'. Fringe field indicated with red 'B'.

While the magnetic field is only necessary for imaging within the scanner bore, it extends outside of the machine into the surrounding area. The external field is termed the fringe field and is indicated with the letter B in Figure 3. In an attempt to minimize the strength of the fringe field for safety purposes, most modern scanners utilize a method called active shielding. In active shielding another set of coils external to the superconductor and other imaging coils create a weak magnetic field in the opposite direction (positive Z). The weak field is not strong enough to make a noticeable impact on the field within the bore, but it is enough to almost eliminate the fringe field [2]. However, the negation of the fringe field increases the magnitude of the spatial gradient at the entrance of the bore as the change in field strength is increased.

2.2. Methods

2.2.1. Equipment

2.2.1.1. Siemens Magnetom Trio

The testing done for this paper was all conducted on a Siemens Magnetom Trio 3T MRI scanner. The results of this thesis are specific to the individual scanner used in this study. However, the methodology and tools developed may be applied to other MRI scanner systems.

2.2.1.2. AlphaLab Gaussmeter Model VGM

The measurements of the static magnetic field were taken using AlphaLab Gaussmeter Model VGM, which consists of a user interface console and a measurement probe. When this probe is placed within a magnetic field, it senses a voltage across two of its parallel faces. This voltage difference is directly proportional to the magnetic flux

density, which is the characteristic of interest for this study [6]. The probe, which is shown in Figure 4, has a triangular notch in the corner of the probe to indicate its correct orientation. The probe lacks an accelerometer so maintaining the correct orientation of the probe is crucial for obtaining consistent results.

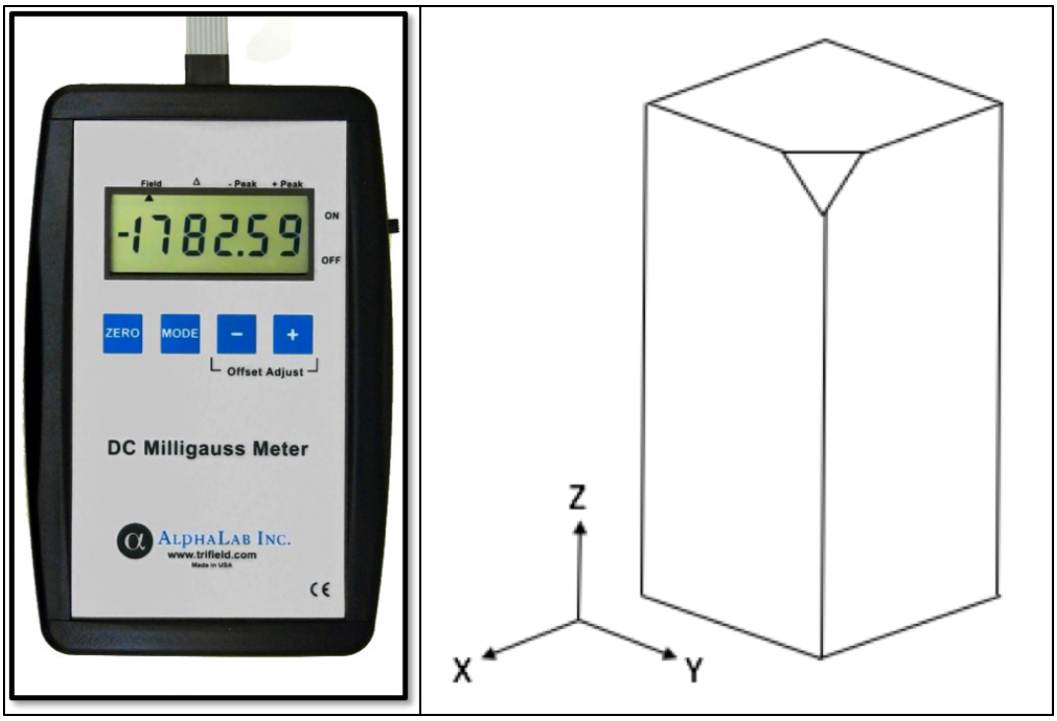

Figure 4: (Left) AlphaLab gaussmeter console (taken from www.trifield.com). (Right) Schematic of gaussmeter probe with the correct orientation indicated by the small triangular notch in the corner.

In the current measurements taken during ASTM 2052 testing, the individual vector components are ignored and only the magnitude is recorded. This simplification, along with the reduced number of measurements, allows the user to manually record the values in a spreadsheet. For the purposes of this study, the X, Y, and Z vector components need to be recorded making the process impractical to complete manually. Although the X and Y components of the magnetic field vector are theoretically

negligible compared to the Z component, it is necessary to measure in all three axial directions to confirm that this assumption is experimentally relevant [2]. AlphaLab has a corresponding application called the AlphaApp. This application is free to download through the AlphaLab website. The gaussmeter can be connected to a laptop using a USB cord, and synced with the application. The application allows the user to automatically record measurements at a specified time interval. The data can be saved and viewed within the application or exported as a text file.

2.2.2. Repeatability Measurements

Before attempting to characterize the entire magnetic field present inside the bore, initial measurements were taken along the z-axis of the scanner to determine if measurements would vary at fixed coordinates. This was determined using only the Alphalab 3-Axis Gaussmeter Probe and the MRI scanner. The gaussmeter was fixed in the center of the scanner bed aimed in the negative z direction, allowing measurements to be observed along the Z-axis only. Measurements were recorded from -100cm to 100cm in the following increments: 10cm increments from -100 to -50cm and 50 to 100cm, 5cm increments from -50 to -30cm and 30 to 50cm, and 1cm increments from -30 to 30cm (all along the Z-axis). This schematic puts the finest focus on the region of interest, the area around the entrance of the scanner bore where the maximum spatial gradient is typically reported [4, 7]. These measurements were taken in triplicate and the results of each round of measurements were plotted against each other for comparison. A one-way ANOVA was completed to identify any discrepancies within the three sets of data.

2.2.3. Fixture Design

A fixture was designed to record repeatable gauss measurements throughout the MRI bore at set coordinates in a reliable fashion. The featured design went through two iterations, with the second being the final product. The design consists of two separate pieces; a circular plate and a base, both of which are made of Delrin® Acetal Plastic (chosen for its magnetically inert properties). The plate contains a number of slots which are designed to fit the gaussmeter probe, each having known X and Y coordinates. The fixture, which can be seen in Figure 5, allows for measurements to be made at designated locations throughout the scanner bore. The dimensions for the designed fixture can be found in Appendix A.

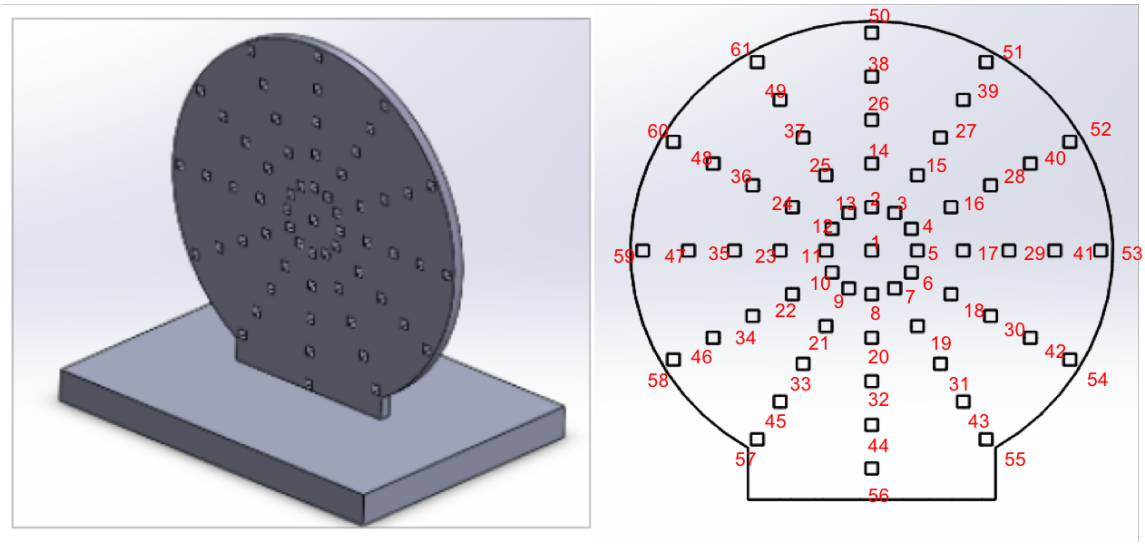

Figure 5: (Left) Three dimensional CAD model of gauss measurement fixture. (Right) Schematic of test locations with corresponding number locations.

2.2.4. Test Procedure

The test protocol created for measuring the spatial gradients of the MRI scanner utilizes the fixture in Figure 5, an Alphalab 3-axis gaussmeter, a laptop, and the MRI scanner. The test fixture is placed on the scanner bed parallel to the face of the MRI scanner in line with the entrance of the scanner bore (this serves as z = 0). A laptop loaded with the AlphaApp along with the gaussmeter is set up just outside the door of the scanner room in order prevent damage to either device. The entire test set up is shown in Figure 7 below.

Figure 6: The test fixture is shown in its proper orientation at the entrance of the scanner bore. The gaussmeter probe is inserted into the first test location slot at the center of the fixture.

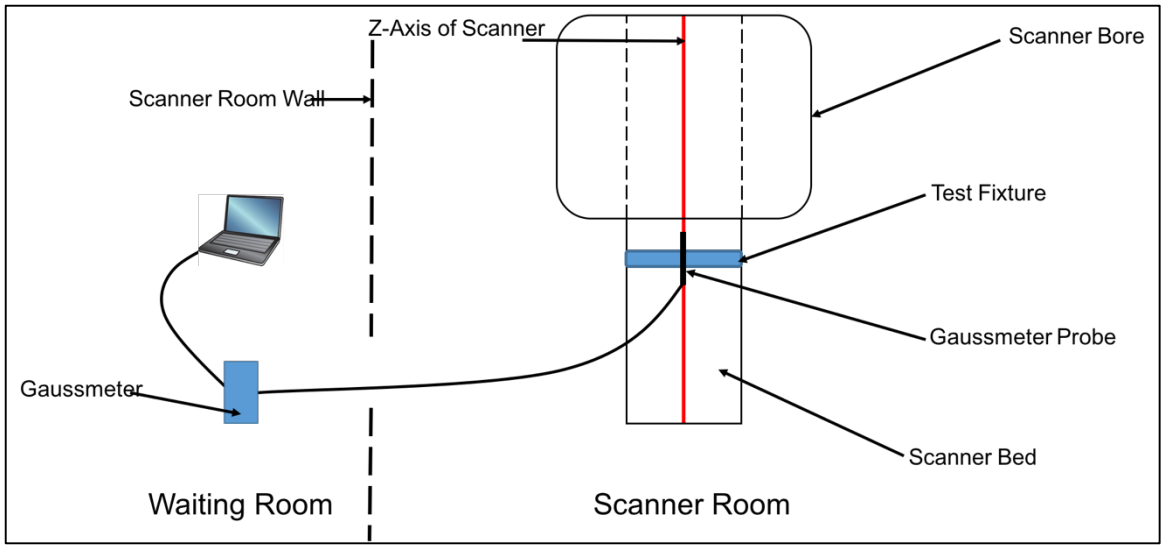

Figure 7: Top-down schematic of the test set up for spatial gradient measurement.

The AlphaApp was programmed to take a measurement automatically every ten seconds. The gaussmeter probe was inserted in the first location of the test fixture and the start button was selected on the application. After each measurement was recorded, the user moved the gaussmeter probe to the next test location. It was imperative for the user to maintain the correct test order so that each recorded measurement could be associated with its appropriate test location at a later time. Once the final recording was measured (location #61), the user stopped the recording and downloaded the data set with the file named for its z coordinate (example: 5cm). The fixture remained in the same position on the scanner bed. The bed was then adjusted to move the fixture to its next z location. This process was repeated for -50cm to 25cm in the z direction using 5cm increments. The procedure yielded a number of text files, each comprised of magnetic field vector measurements at multiple X & Y coordinates at a singular Z location.

2.2.5. Importation into COMSOL

The data collected through the experimental procedure described above was concatenated into a single spreadsheet using Microsoft Excel. The first three columns of the spreadsheet designated the X, Y, and Z spatial coordinates while the second three columns corresponded to the X, Y, and Z vector components of the magnetic vector, which will now be referred to as Bx, By, and Bz. The units for the spatial arguments were converted from centimeters to meters, while the units for the vector components were converted from Gauss to Tesla. The completed spreadsheet, which is now a point cloud of data, could then be imported into COMSOL Multiphysics. The point cloud of measurements can be seen in Figure 8 below.

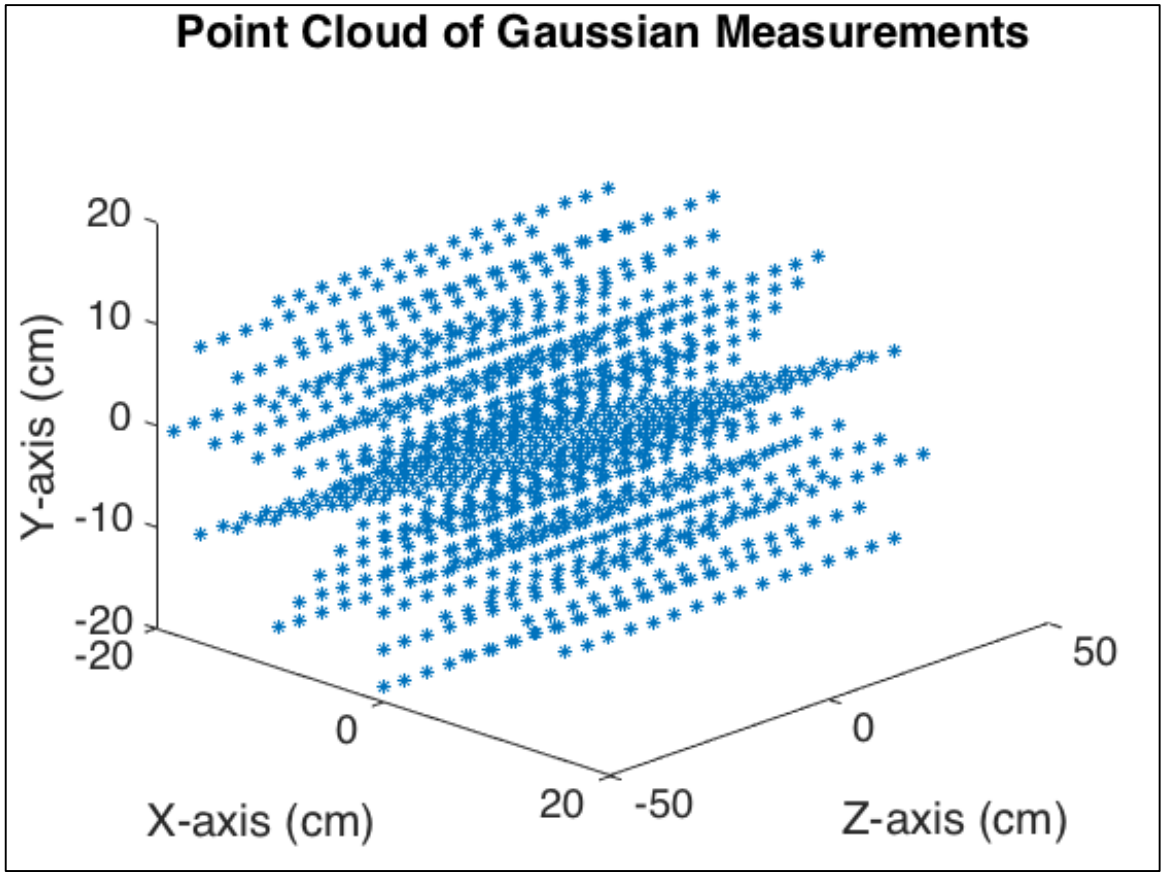

Figure 8: The point cloud of measurements experimentally measured using the designed test fixture. Each dot represents one measurement with X, Y, and Z vector components.

COMSOL provides its users with the capability to define their own functions to call throughout their simulations. The interpolation function was used to import the master spreadsheet containing the spatial coordinates and magnetic field vector measurements. The function linearly interpolates the data in between each XY planar slice to create continuous field vectors throughout the space of interest. Each vector component of the magnetic field is assigned its own function name (Bx, By, Bz) that can be called later by the user's simulation. The default extrapolation setting is left as constant extrapolation and can be ignored since no samples will ever be placed outside of the measurement region.

2.3. Results

2.3.1. Preliminary Results

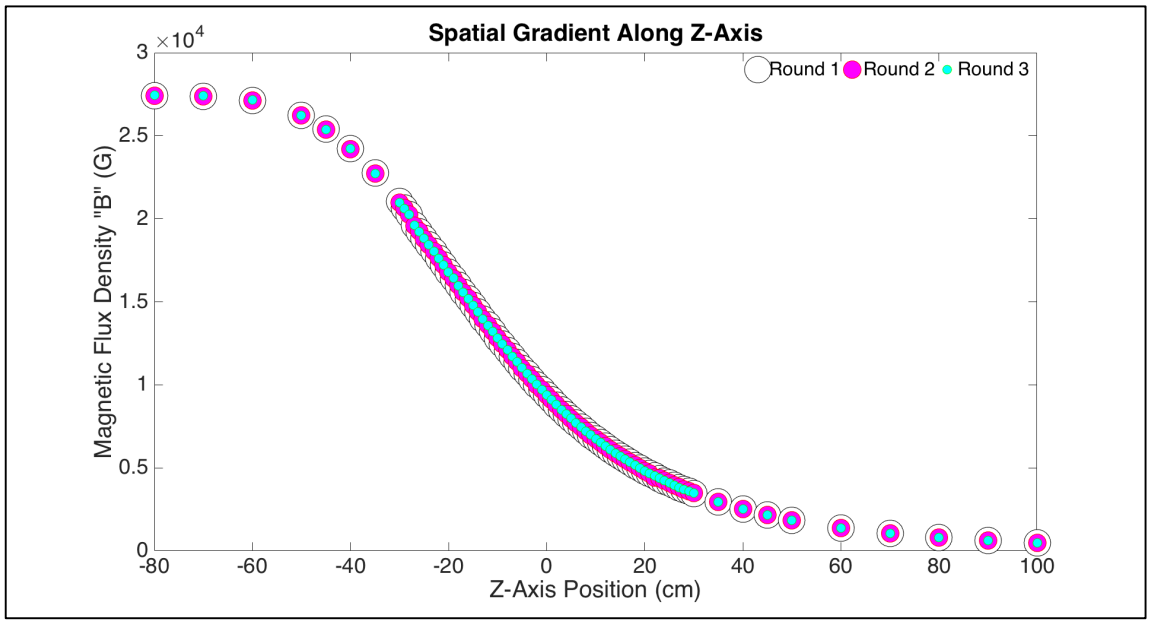

Figure 9: Initial gaussian measurements taken with fixed X & Y coordinates along the Z-axis of the scanner bore. Z = 0 indicates the entrance of the MRI scanner bore.

The three different sets of measurements were plotted on the same axes to give a visual representation of the repeatability of the measurements. The one-way ANOVA returned a p-value of 1, indicating that there was no significant difference between each group of measurements. The full results of the one-way ANOVA can be found in Appendix B.

2.3.2. Final Results

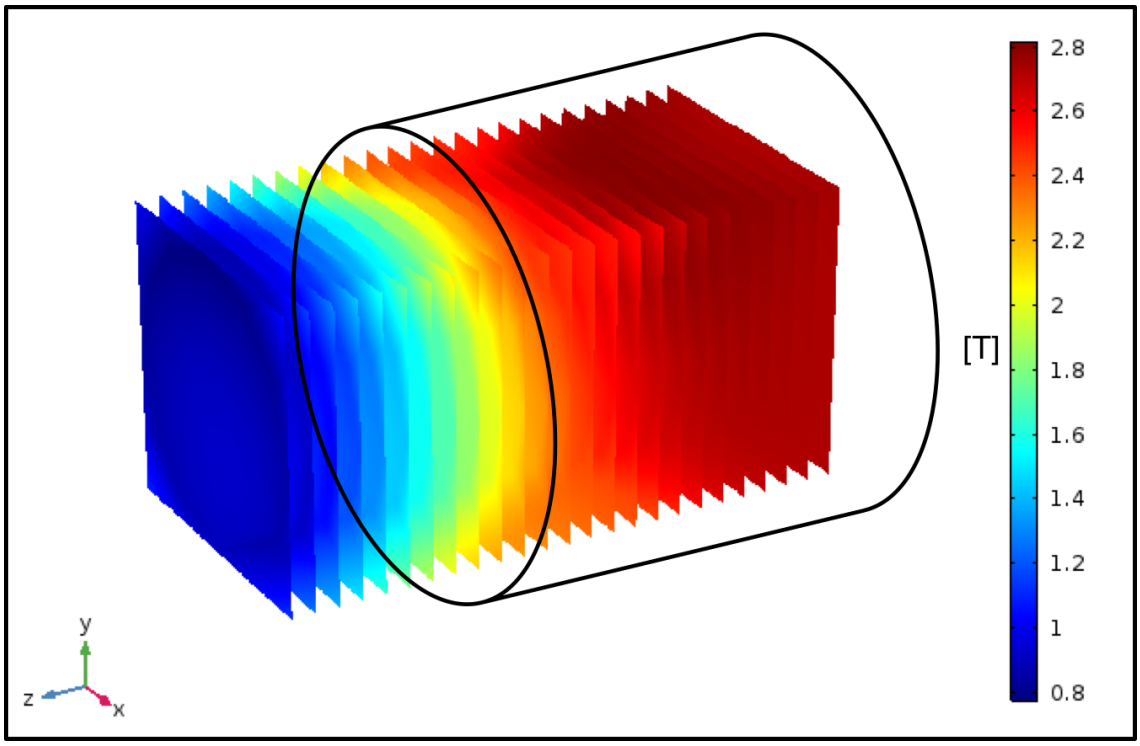

Figure 10: Final Gaussian measurements shown using XY planar slices of the interpolated data. In this image, the data has not been interpolated in the Z-direction, but instead within the XY plane at each given Z – location. A cylinder is superimposed on the planar slices to indicate the spatial relationship with the MRI scanner bore.

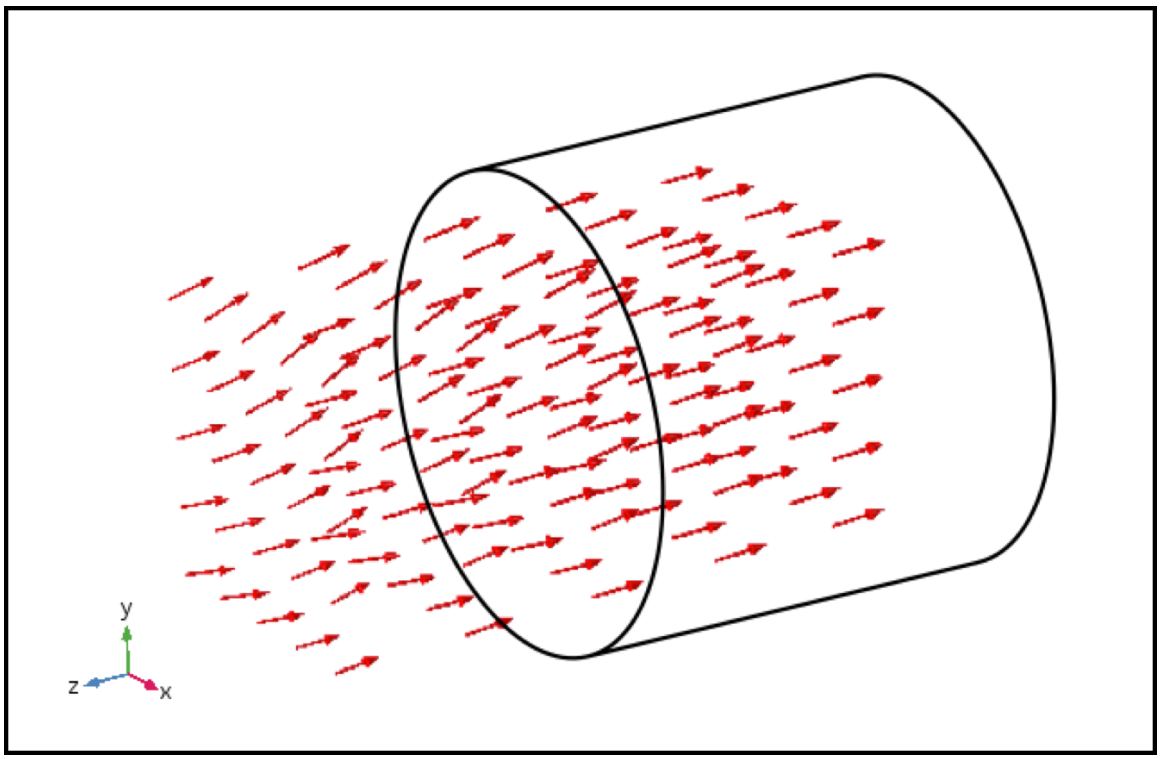

Figure 11: Final results of measured magnetic field represented by a field of vector arrows. This representation demonstrates the interpolation in the X, Y, and Z directions. A cylinder is superimposed on the vector arrows to indicate the spatial relationship with the MRI scanner bore.

Figure 10 shows the results of the interpolation function of the static field measurements. The results are represented as a series of XY planar slices along the length of the MRI bore. Figure 11 includes a series of vector arrows indicating the direction of the magnetic field. The direction of the vector arrows helps validate the assumption that the direction of the current creating the magnetic field is into the bore of the scanner. In both Figure 10 and Figure 11 a cylinder was superimposed over the results in order to help understand the positioning of the MRI bore within the magnetic field.

3. Aim 2

3.1. Background

3.1.1. Classification of Magnetic Materials

The magnetic properties of the materials used in medical devices are one of the major contributors to translational forces created by the static magnetic field. In the most general sense, materials can either be classified as either magnetic or non-magnetic. The term non-magnetic is a misconception, however, since all materials are somewhat magnetic in nature. "Non-magnetic", instead, is a relative term indicating that the material properties produce a negligible magnetic effect. The types of magnetism that contribute to a material's magnetic qualification can be described qualitatively with relative ease. For the purposes of this paper, only the three main types of magnetism are discussed.

The first type of magnetism is called diamagnetism and it is present in all forms of matter. According to Lenz's Law, the current induced in a material proceeds in a direction to create a magnetic field opposite to the magnetic field that created the current [8]. This causes the material to be repelled by the induced magnetic field. These diamagnetic effects are usually very weak and are often dominated by other types of magnetism. Materials that only experience this type of magnetism are classified as diamagnetic materials [9, 10].

The next type of magnetism is referred to as paramagnetism. Paramagnetism, unlike diamagnetism, results in the attraction of a material in the direction of an applied magnetic field. This action is a result of the paramagnetic properties of a material beginning at the atomic level with each individual atom's electrons. An electron proceeds around the nucleus in a fixed orbit, which can essentially be viewed as a circular

loop. Since an electron holds an inherent charge it creates a current along its orbit. A magnetic moment (m) is a vector product of the current created by the electron (I) and the electron's angular momentum (A) as shown in Equation 1.

$$m = IA \tag{1}$$

Paramagnetism is exhibited by atoms or molecules that have free electrons or an unfilled valence shell. In the absence of an applied magnetic field, the directions of all the magnetic moments within a material's atoms or molecules are randomized and usually cancel out causing the substance to appear "non-magnetic". However, when a magnetic field is applied the magnetic moments tends to align themselves parallel to the field, causing the material to be magnetized in that direction. Paramagnetic materials are those in which the effects of diamagnetism are overshadowed by the paramagnetic effects although these affects are respectively minimal as well [9, 11].

Ferromagnetism, the third form of magnetism, is similar to paramagnetism in that it contributes its properties to net magnetic moments of its atoms or molecules. However, ferromagnetic materials do not necessarily need an applied magnetic field to become magnetized. Ferromagnetic materials possess regions called domains that have their own net magnetic moment. The directions of the moments of the various domains within a magnetic material are not necessarily uniform and therefore a ferromagnetic material may not be magnetized [9]. The different domains within a region, however, have the power to influence each other which can cause spontaneous magnetization of a material. Ferromagnetic materials are those that are typically viewed as magnet, of which there are two types; hard and soft magnets. Hard magnets, also known as permanent magnets, are difficult to magnetize or demagnetize. Hard magnets are generally avoided in MRI

applications and therefore are not relevant for the purposes of this paper. Soft magnets are easily magnetized with an applied field and demagnetize fairly easily with the removal of that field [12]. Soft magnetic materials are more commonly found in the types of devices that could potentially be introduced to the MRI environment and therefore are the ones examined in this paper.

While the qualitative definitions of these magnetic classes are useful for understanding how a material will behave when introduced to a magnetic field, they fail to address the severity of these reactions. A better understanding of how much a material will interact with a magnetic field requires a quantitative measure. In the case of magnetization of materials, magnetic susceptibility (χ) and relative permeability (μ_r) are the two properties that are used are quantitative measures.

3.1.2. Magnetic Susceptibility and Relative Permeability

The magnetic susceptibility describes the magnetization of a material at a given magnetic field strength (H) [9, 13]. This relationship is described in Equation 2 below. Similarly, the permeability relates magnetic flux density (B) with magnetic field strength (Equation 3) [4].

$$M = \chi H \quad [2]$$

$$B = \mu H \quad [3]$$

Magnetic susceptibility and permeability can be related through the relative permeability (μ_r) which can be calculated using the equation, $\mu_r = \frac{\mu}{\mu_o}$, where μ_o is the permeability of free space. The relationship between magnetic susceptibility can be found using Equation 4 through steps a-e below [2, 4].

a. $$B = \mu_o(H + M) \quad [4]$$

b. $$\mu H = \mu_o(H + \chi H)$$

c. $$\frac{\mu}{\mu_o} H = H(1 + \chi)$$

d. $$\frac{\mu}{\mu_o} = (1 + \chi)$$

e. $$\chi = \mu_r - 1 \quad [5]$$

Both magnetic susceptibility and relative permeability are dimensionless (lack units) in the SI system can be used almost interchangeably due to their simple relationship.

A material's magnetic properties are usually designated based on its magnetic susceptibility. Diamagnetic materials have magnetic susceptibilities ranging from negative one to zero (the minimum magnet susceptibility is negative one). The negative magnetic susceptibility is due to the material's tendency to be repelled in the opposite direction of the magnetic field [2]. Paramagnetic materials have a positive magnetic susceptibility that is less than 0.01. Paramagnetic materials encompass the majority of the materials on Earth, including biological tissue. While the magnetic susceptibilities of paramagnetic materials may be positive, they are generally too small to observe any macroscopic effects, except in extremely high strength magnetic fields. The magnetic susceptibilities of both diamagnetic and paramagnetic materials are small enough that they are often perceived as "non-magnetic" [2].

Ferromagnetic materials are indicated by a positive magnetic susceptibility greater than 0.01 [2, 14]. The boundary between paramagnetism and ferromagnetism at 0.01 is not a definitive cutoff value, but rather serves as a general rule of thumb. While

magnetic susceptibility is a constant value for diamagnetic and paramagnetic materials, it varies for ferromagnetic materials due to the magnetic domains within the material. Depending on the strength of the applied field, the direction of the magnetic moments within each domain are altered resulting in varying levels of magnetization (translating into different values for magnetic susceptibility and relative permeability) [14]. The possible domain alterations as a result of an applied magnetic field are summarized in Figure 12.

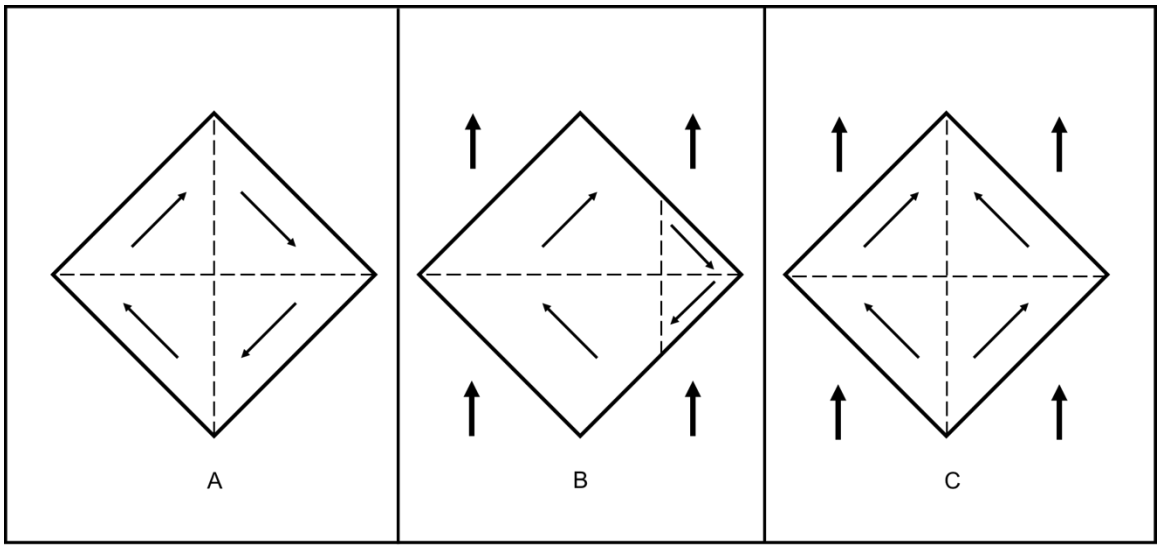

Figure 12: Different cases showcasing the direction of the magnetic moments in the domains of a ferromagnetic material. There is no applied magnetic field in A, however, there is an applied field in both B and C (indicated by the bold vertical arrows) Figured adapted from [14].

The diamond shaped regions represent the body of ferromagnetic material with its respective boundaries separated by dotted lines. Case A of Figure 12 shows a material in the absence of an applied magnetic field where the directions of the magnetic moments (indicated by the solid arrows within each subsection of the diamond) are random and

result in zero magnetization. Case B indicates a situation in which the material is exposed to a magnetic field resulting in the boundaries of the domains to change. This modification to the boundaries of the domain changes the size of the various domains which effectively changes the number of atoms sharing the same magnetic moment direction. This results in breaking the equilibrium of magnetic moments and thus magnetizing the material. Case C is another situation in which a magnetic field is applied to the material. In this case, however, the boundaries of the domain remain the same, but the domains themselves rotate and change the direction of their magnetic moment. Case B tends to occur at lesser strength magnetic fields, while Case C begins to occur as the strength increases. A common method of observing the change in magnetization with increasing field strength is to plot the relative permeability against magnetic flux density (Figure 13). From this graph the magnetic susceptibility can be calculated for a given value of B using Equation 5.

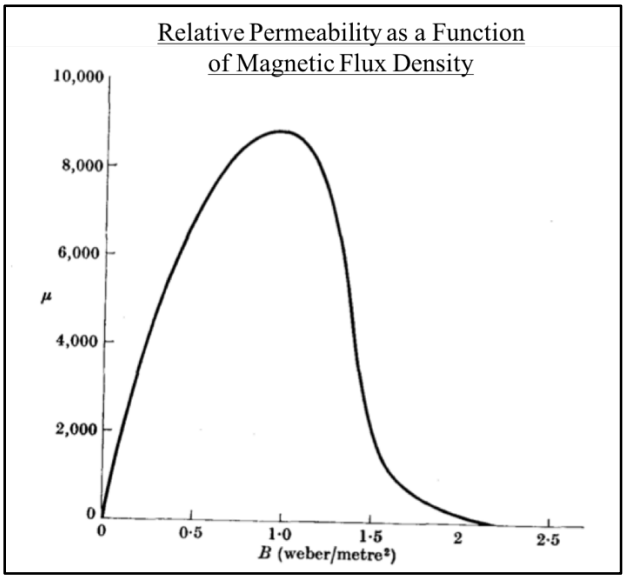

Figure 13: Permeability vs. B for iron. Plot adapted from [14].

3.2. Methods

3.2.1. Experimental Testing

3.2.1.1. Sample Preparation

The sample was modeled as a solid polyurethane cylinder with a tapped hole running along its center axis beginning at one face of the cylinder. This hole extended approximately 85% of the entire length of the sample in order to create a pocket in which varying amounts of steel beads could be inserted. The engineering drawing with exact measurements of the sample model can be seen in Appendix A. The cylinder was manufactured using Smooth-Cast® 300Q liquid plastic, which is a two-part polyurethane casting resin. Equal portions of each component were poured into a plastic cup, mixed thoroughly, and allowed to cure for approximately ten minutes resulting in a block of bright white polyurethane. The block was then turned down to its desired radius and length using a lathe. A small horizontal notch was made using the lathe along the midline of the sample. This provided the user a securing point for the string used for experimental testing. A hole was drilled in the center of the top face of the sample using a drill press. This hole was tapped with a M6 x 1.0 thread designation along the entire length of the hole. An M6 x 1.0 nylon hex head screw was then used to seal the pocket of the sample. Both polyurethane and nylon were chosen for this sample because they are largely unaffected by a magnetic field due to their material properties (reference needed). The final sample can be seen in Figure 14 below.

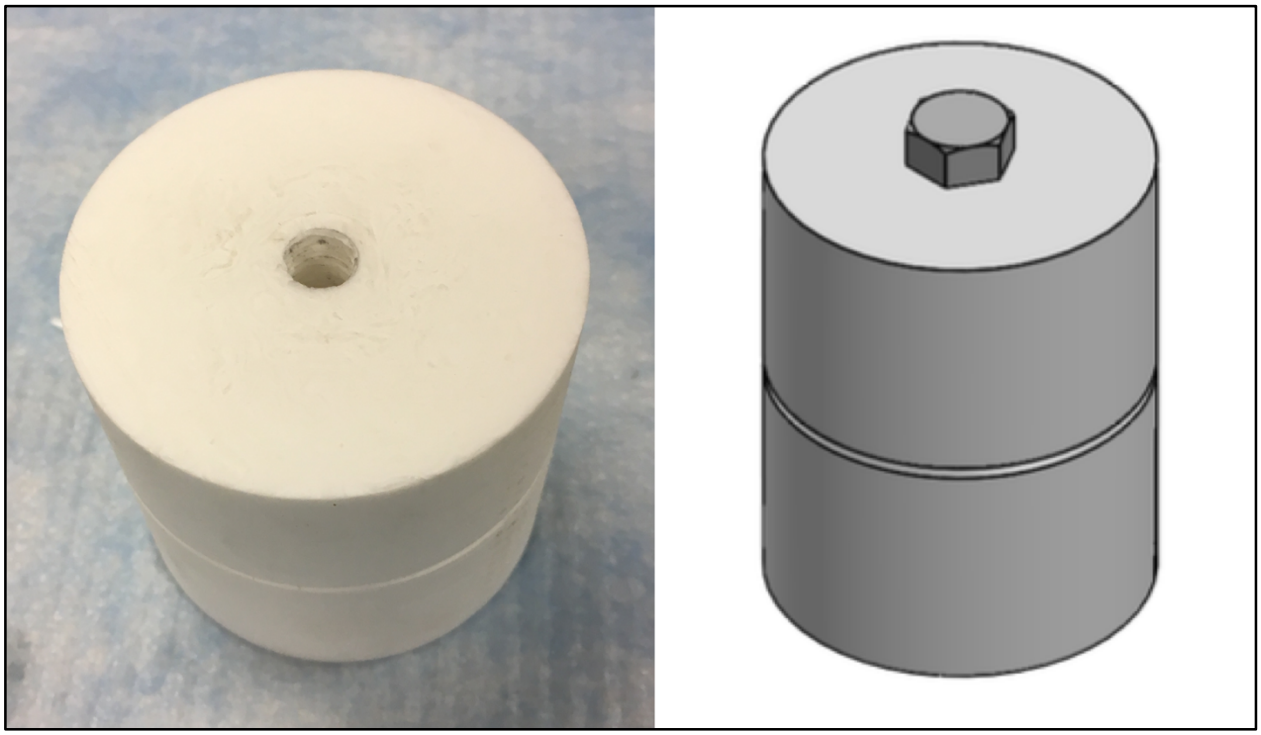

Figure 14: (Left) Final experimental test sample without the nylon screw. (Right) Three dimensional model of test sample.

Low-carbon steel was chosen as the material to fill the hollow polyurethane vessel for its ferromagnetic properties [15]. Steel beads with radii of 1/16" were counted and bagged in increments of 5 from 5 to 80 beads with additional bags of 90 and 100 beads, totaling eighteen samples. Gravimetric measurements of each sample as well as the polyurethane block (including the nylon screw) were taken in triplicate and their mass ratios were calculated. The gravimetric averages and resulting mass ratios of each sample can be seen in *Table 1* below.

Table 1: Gravimetric measurements of low-carbon steel bead samples. Mass ratios calculated using an average polyurethane mass of 69.36441 grams.

Sample	Number of Beads	Average Mass (g)	Mass Ratio (%)
1	5	0.08126	0.117
2	10	0.16641	0.240
3	15	0.24823	0.358
4	20	0.33001	0.476
5	25	0.41237	0.594
6	30	0.49621	0.715
7	35	0.57875	0.834
8	40	0.65830	0.949
9	45	0.74513	1.074
10	50	0.82800	1.194
11	55	0.90930	1.311
12	60	0.97386	1.404
13	65	1.07590	1.551
14	70	1.15759	1.669
15	75	1.23836	1.785
16	80	1.32109	1.905
17	90	1.48651	2.143
18	100	1.59880	2.305

3.2.1.2. Test Procedure

The testing protocol used for this experiment was adapted from a standard operating procedure written and developed by Exponent Failure Analysis Associates, which was based on of ASTM 2052-15. All testing fixtures and equipment were designed and provided by Exponent. The test fixture, which can be seen in Figure 15, is made entirely of nylon making it magnetically inert and consists of a solid rectangular base and a singular post with a notch along its vertical axis. On this post exists a protractor with a pin protruding perpendicularly from its center.

Since displacement force is caused by the spatial gradients of the static magnetic field, the test is performed at the point where maximal spatial gradient has been reported. This point occurs at 0 cm in the x-direction, half the bore diameter in the y-direction, and 99cm from isocenter in the z-direction. The fixture is positioned on the scanner bed so that the center of the post is located at z = 99cm. The face of the protractor is perpendicular to the entrance of the scanner bore so that the user can read the values of angular displacement. The sample described above is suspended from the pin of the fixture with a string at a height equal to half of the bore diameter. This experimental set up can be seen in Figure 15 below.

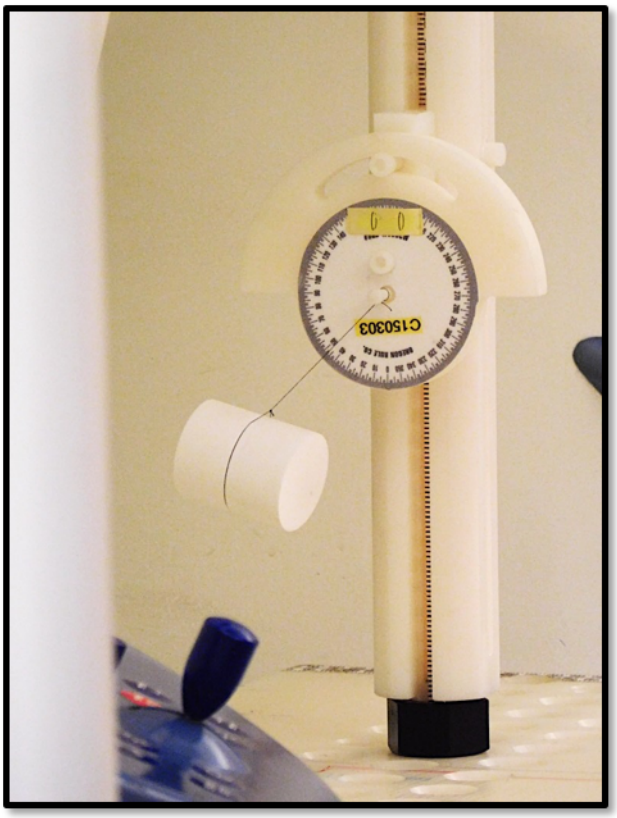

Figure 15: Test set up for measuring magnetically induced displacement force as described in ASTM 2052-15 (reference).

Beginning with an empty vessel, the sample is allowed to hang from the fixture until coming to rest. Using the protractor on the fixture, the angular displacement is measured in degrees and recorded. The pin of the fixture is then removed with the sample still attached and removed from the scanner room so that beads can be placed in the sample outside of the magnet's influence. The pin was removed from the fixture as opposed to removing the string from the pin in order to maintain the same height of the sample throughout the entirety of the experiment. Once safely outside the scanner room the nylon screw can be removed and the next sample (bag of steel beads) can be emptied into the sample. After the nylon screw is replaced and the pin reinserted into the fixture, the next measurement can be recorded. This process was repeated for each sample three times and their averages and standard deviations were calculated.

3.2.2. COMSOL Simulation

COMSOL Multiphysics was selected to create the model for this thesis based on its ability to easily couple multiple physics domains, its user-friendly interface, and its ability to seamlessly interface with other programs such as MATLAB, Excel, and Solidworks. This model was initiated using COMSOL's Model Wizard, which helps the user set up their simulation by automatically coupling different physics modules with the appropriate equations. The Solid Mechanics module was selected as the primary physics application for the simulation. Although the RF (Radiofrequency) module is typically used for most MRI applications, it is unnecessary for this model since the magnetic field does not need to be generated by the software. Instead, the magnetic field was measured experimentally and imported into COMSOL as an interpolation function (described in

section 2.2.5 above). The Stationary Study was selected as the results of the simulation are not time dependent.

3.2.2.1. Geometry – Verification Model

The geometry of the verification model was designed to replicate the testing described in ASTM 2052-15 using the verification samples that were described above in section 3.2.1.1. The final geometry used in the verification model is shown in Figure 16 below.

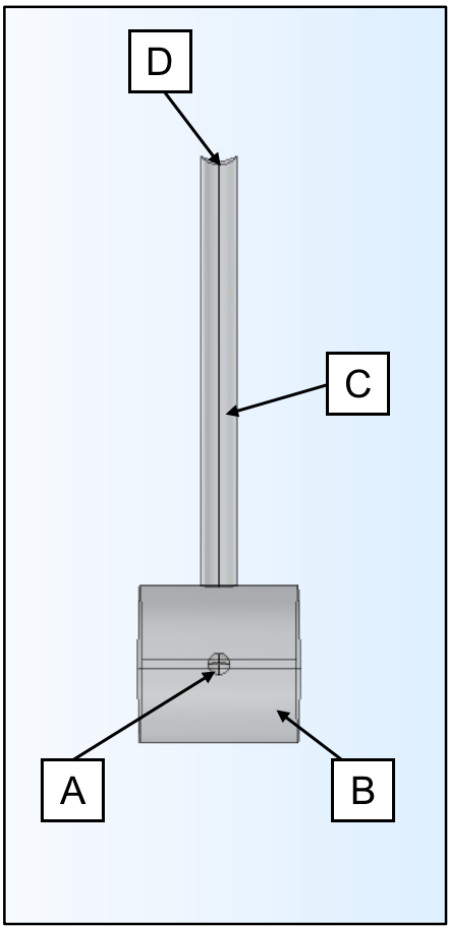

Figure 16: Final geometry for verification model. The markers indicate the following structures: A - low-carbon steel ball, B - polyurethane cylinder, C - nylon "string", D - location of spring foundation mimicking fixture.

The major features of the model are indicated using alphabetical markers in Figure 16. In order to simplify the experimental test setup to the final geometry displayed above, a number of assumptions were made. The first assumption simplified the multiple steel beads within the sample to a single steel sphere embedded at the center of the polyurethane block (indicated as B in Figure 16). The radius of the modeled sphere was calculated from the gravimetric measurements in Table 1 using Equations 6 and 7 (volume of a sphere) where V is volume, m is mass, ρ is density of the material, and r is the radius.

$$m = \rho V \quad [6]$$

$$V = \pi r^3 \quad [7]$$

The string that the experimental samples are normally suspended from were transitioned to a nylon cylinder (labeled C in Figure 16). The thin diameter of the string created convergence issues within the model and was too computationally heavy to mesh. Therefore, it was replaced with a thicker cylinder made of nylon, allowing it to remain unaffected by the magnetic field. Gravity was applied in the negative y direction on both the steel sphere and the polyurethane cylinder. The nylon cylinder was not included since the string has a negligible mass and does not contribute to the overall gravitational force experienced by the sample. The nylon fixture featured in Figure 15 that is used for experimental testing is mostly neglected in this model. The role of the fixture is substituted by a spring foundation placed on the surfaces at the top of the string (labeled D in Figure 16). The spring foundation node will be discussed in further detail later in section 3.2.2.6. The steel ball, polyurethane cylinder, and string are all modeled as rigid domains, meaning that their geometries cannot deform as a result of an applied force.

This is yet another simplification that allows the simulation to reallocate its computational power elsewhere.

3.2.2.3. Materials

The materials selected for this model were all chosen based on their magnetic properties. For the verification model, nylon and polyurethane were chosen for their paramagnetic nature, while low-carbon steel was chosen for its high magnetic susceptibility. The materials for the medical device model were selected based on materials used in devices currently on the market. The full list of the materials along with their relevant material properties can be found in Table 2 below.

Table 2: Material properties of the materials utilized in the simulation [15, 16].

Material	**Density (kg/m^3)**	**Elastic Modulus (Pa)**	**Poisson's Ratio**	**Magnetic Susceptibility**
Nylon	1150.00	2e9	0.40	<<0.01
Polyurethane	1049.07	9.6e8	0.48	<<0.01
Low-Carbon Steel	7833.41	205e9	0.29	1 - 300

As shown in Table 1 the magnetic susceptibility of low carbon steel is a range of values rather than a constant. This range was obtained from the graph of relative permeability as a function of magnetic field strength shown in Figure 17.

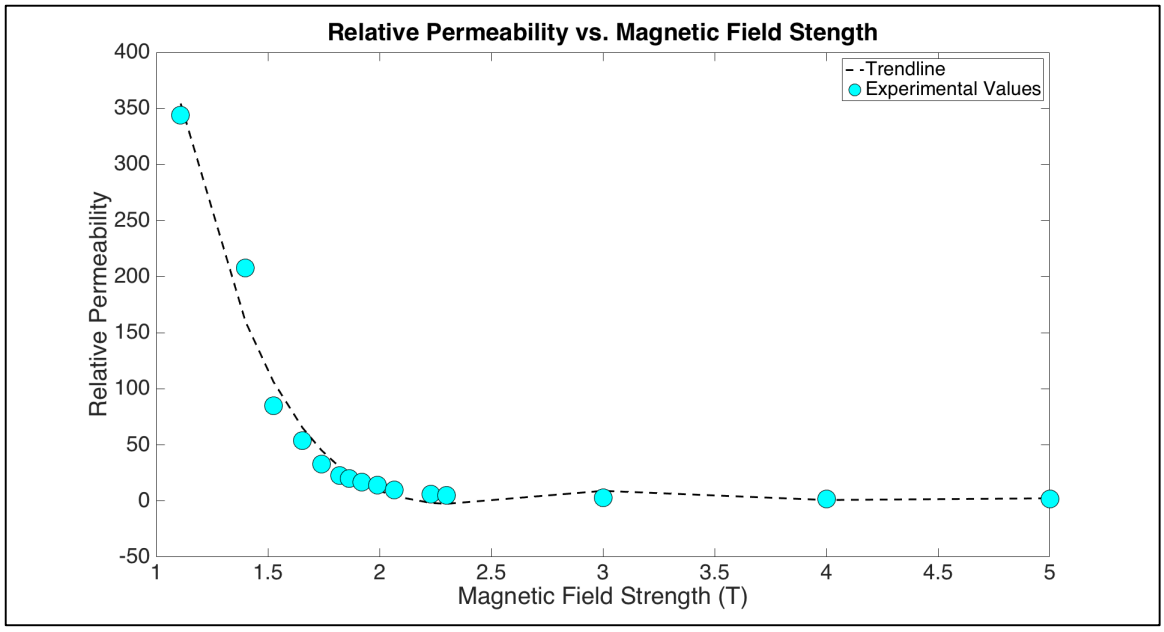

Figure 17: Relative permeability as a function of magnetic field strength for low-carbon steel. The experimentally gathered data points shown in blue were obtained from [15].

Equation 8 is the equation of the trend line shown in Figure 17 and was used to calculate the relative permeability and ultimately the magnetic susceptibility at a given field strength.

$$y = -4.576x^5 + 88.544x^4 - 664.63x^3 + 2411.8x^2 - 4220.8x + 2850.1 \quad [8]$$

3.2.2.5. Force Calculation

In experimental testing, the magnetically induced displacement force (F_m) is usually calculated based on the angular displacement measured during testing per ASTM 2052. F_m is calculated experimentally using equation X where ρ is density of the device material, V is the volume of the device, g is gravity in the negative y direction, and θ is the angular displacement of the sample.

$$|F_m| = \rho V g \cdot \tan(\theta) \quad [8]$$

The magnitude of the magnetically induced displacement force on a device is dependent on the magnetic susceptibility of the device's material, the strength of the field, and the spatial gradient of the magnetic field. The full equation of displacement force is shown below in Equation 9.

$$F_m = \frac{V\chi}{\mu_o} |\boldsymbol{B}_o| \cdot \left|\nabla |\boldsymbol{B}_o|\right| \quad [9]$$

V is the volume of the device, χ is the magnetic susceptibility, μ_o is the permeability of free space ($4\pi \times 10^{-7} H/M$), $\mathbf{B_o}$ is the vector of the static magnetic field, and $\nabla \boldsymbol{B_o}$ is the gradient vector of the static magnetic field. Since the vector components of the magnetic field in the X and Y directions are essentially negligible compared to the Z component of the vector, $\nabla |\boldsymbol{B_o}| = \frac{dB_o}{dz}$ resulting in Equation 10.

$$F_m = \frac{V\chi}{\mu_o} |\boldsymbol{B}_o| \cdot \left|\frac{dB_o}{dz}\right| \quad [10]$$

Equation X was used to calculate the force as a result of the sample being placed within the static magnetic field. This force was applied over the entire geometry to the sample similar to the gravitational force applied to a mass. F_m was applied at each node in the mesh of the device in the negative Z direction.

Due to the nonlinear nature of the model, the implementation of the force equation results in convergence issues that were addressed through the use of an auxiliary parameter sweep. A generic parameter, *para*, was inserted into Equation X to produce Equation 11 below.

$$F_m = para * \left(\frac{V\chi}{\mu_o} |\boldsymbol{B}_o| \cdot \left|\frac{dB_o}{dz}\right|\right) \quad [11]$$

This parameter was applied in sequential steps of 0.1 from 0 to 1. The final step when *para* = 1 would result in the full amount of force being applied to the component. Applying the load in smaller increments allows the solver to use each previous step as a closer initial condition to base its solution upon. This method, which is also known as the continuation method, improves the robustness of the model.

3.2.2.5. Angular Displacement Measurement

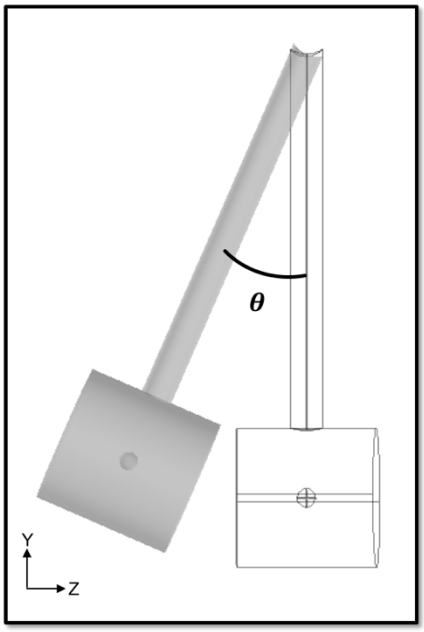

Figure 18: Angular displacement of the verification sample in the YZ plane. The angular displacement is designated as theta.

The final output of the model is the angular displacement, theta (θ), of the verification sample. Theta is measured as the angle between the central axis of the string (C in Figure 16) and the vertical Y axis.

3.2.2.6. Spring Stiffness Optimization

The spring foundation located at the top of the string within the model (labelled D in Figure 16) is an essential tuning parameter for the accuracy of the model. In reality, no spring exists at the top of the string, but the spring foundation serves as a correction factor. When the magnetically induced displacement force is applied to the sample, the model tends to oscillate around the target displacement, overshooting then undershooting, overshooting etc. These oscillations take time and exceeding amounts of computational power, sometimes resulting in convergence issues within the model. In order to select the correct spring stiffness constant a parametric sweep was conducted across a range of values. Each set of simulated data was plotted on the same graph along with the experimental values, which can be seen in Figure 19.

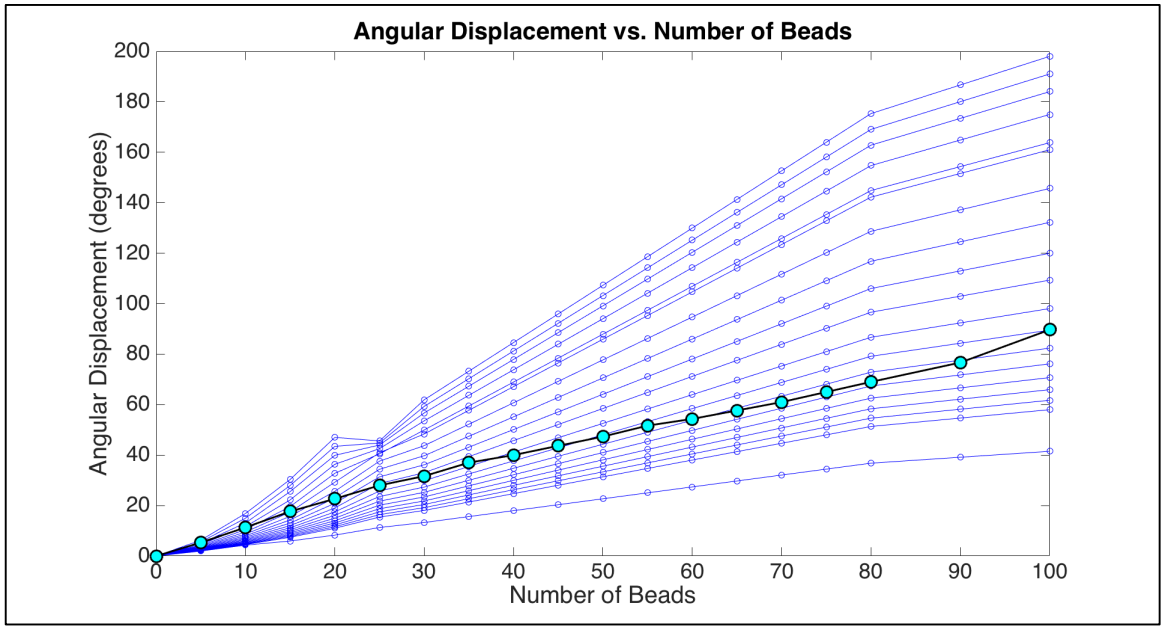

Figure 19: Parameter estimation for the spring stiffness constant used in the spring foundation of the model. Each thin blue line represents a different stiffness coefficient. The experimental data is represented by the bold black line with line blue circles.

The set of simulated results that best represented the experimental data was chosen based on the graph above. The spring constant for that set, k = 2.1e10, was selected as the spring constant for the rest of the results.

3.3. Results

3.3.1. Experimental Results

The angular displacement (measured in degrees) is expressed as a function of the number of beads used in the sample, which can be seen in Figure XX below.

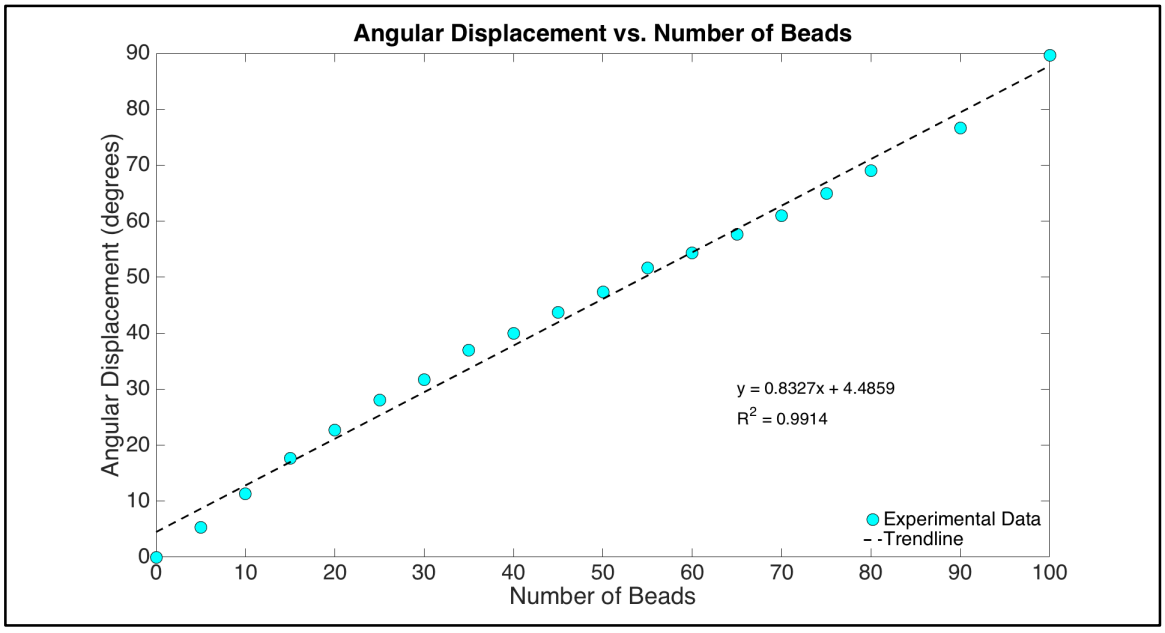

Figure 20: The experimental data collected using the verification sample. The angular displacement of the sample shows a linear relationship with the number of beads used within the verification sample.

A line of best fit was applied to the graph of the angular displacement results. The coefficient of determination for this fitted line is 0.9914, indicating that the line is a good

statistical representation of the collected data. The equation for this line is shown in Equation 12 below.

$$y = 0.8327x + 4.4859 \quad [12]$$

Full results of the experimental testing can be found in Table 3 of Appendix C.

3.3.2. COMSOL Simulation Results

The final results of the COMSOL simulation can be found below in Figure 21 plotted on the same axes as the experimentally gathered data.

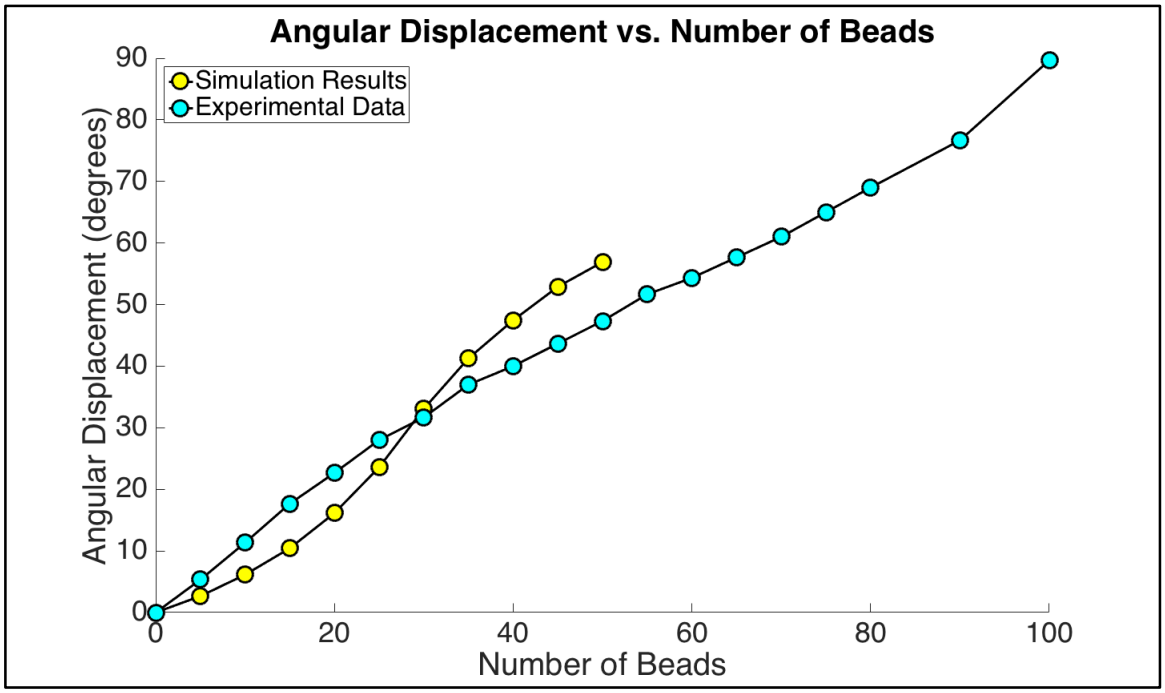

Figure 21: The final results of the COMSOL simulation (yellow) compared with the experimentally gathered data (blue).

The simulation undershoots the experimental values when the number of beads ranges from 0-30 and overshoots when there are greater than 30 beads present in the verification

sample. The absolute error between the two sets of data ranges from 1.4 to 9.6 degrees resulting in a relative error between 4 and 50 percent. The full results can be found in Appendix C. The simulation results stop after the number of beads reaches 50 beads due to convergence issues within the model. This convergence issue is likely due to hardware constraints and a computationally heavy simulation.

4. Discussion and Conclusions

This Master's thesis consisted of two specific aims centered around furthering the ability of researchers to effectively predict the angular displacement that medical devices experience when placed in a MRI setting. The first of these aims was to create a fixture and methodology capable of measuring the spatial gradients throughout the MRI scanner bore. The second aim was to create a three dimensional simulation using COMSOL Multiphysics software that was capable of replicating the experimental testing specified in ASTM 2052-15. The predictive application created for this research utilizes the data collected from spatial gradient measurements allowing the users to test samples in a realistic magnetic field.

The fixture designed to measure the static magnetic field in the MRI scanner bore successfully fulfilled all of its target design criteria. The fixture was able to travel along the length of the scanner bore with ease and interface with the gaussmeter probe, allowing the user to record repeatable measurements. Although the fixture was able to capture the portion of the magnetic field that most devices encounter within the scanner bore, it is limited to the cylindrical area within the bore and along the scanner bed. If the entire magnetic field within the scanner room needs to be captured, a supplementary fixture will could be conceived to measure the fringe field that extends away from the bore to the periphery of the room.

The final results of the spatial gradient measurements shown in section 2.3.3 above indicate that the fixture and methodology created were successfully able to capture the static magnetic field. Figure 10 and Figure 11 indicate that the direction of the magnetic field proceeds into the bore as one would expect. The strength of the magnetic

field steadily increases further into the bore. The magnitude approaches 3.0 Tesla near the isocenter of the bore, which is theoretically the strongest point of the magnetic field within the bore. These cues within the final results for Aim 1 indicate that the static magnetic field was correctly measured. The efficiency of that method was determined by the amount of time it required to measure a complete field. The method was deemed efficient if the complete field could be measured correctly by a single person within a single day of testing according to the initial success criteria. This target was reached with little difficulty, indicating that all of the success criteria for Aim 1 were met.

The COMSOL simulation was more of a complex endeavor in which not all of the design criteria could be completely met. The simulation needed to be able to accept a specified geometry into the MR environment to recreate the forces that enact upon that geometry. The accuracy of those forces was verified through comparing the angular displacement to a set of experimental data collected using a series of standardized samples. The success criteria for the model was defined as being able to predict angular displacement with ±3 degrees of the experimental data. While the model readily accepted the geometry of the verification sample, not every verification sample could be predicted within the acceptable design criteria. Only 27% of the experimental data points fell within the acceptable region, but this number increased 45% when the acceptance criteria was extended to ±5 degrees of angular displacement. The acceptable range of accuracy for angular displacement is one that has yet to be determined by any regulatory body such as the FDA. Ultimately, the FDA has the final determination on whether or not a device is deemed “MRI Safe”, so the task of defining an acceptable range of accuracy for predictive applications lies in their jurisdiction.

A limitation of the COMSOL simulation is its reliance on the user-defined material properties. The magnetic susceptibilities of the materials used within the simulation drive the forces that act upon the model. Essentially, the entire model depends on the accuracy of those material properties. Unfortunately, the relative permeability or the magnetic susceptibility of materials is not an area that is fully researched. Methods for measuring magnetic susceptibility are challenging and dated. The lack of knowledge surrounding these parameters causes concerns for the success of this predictive application. The performance discussed above might be a result of incorrect material properties. The type of material used in the verification sample could have been misreported leading to an incorrect set of material properties to be used within the COMSOL simulation. This model relied on reported values for necessary material properties which allowed for the possibility of inaccuracy.

Experimental testing of medical devices to determine their safety within a magnetic resonance environment is a costly endeavor, attributed by the significant time and resources required. A predictive application could minimize those costs or, at the very least, prevent unnecessary testing. The aim of this thesis was to help fill that void for one of the several tests conducted on medical devices. Although the application was unable to perfectly predict the angular displacements seen in experimental testing, it made significant steps towards a comprehensive predictive tool. This work has contributed to the continuous improvement of medical device testing in a MR setting not only through the innovative nature of the predictive application, but also through the identification of shortcomings in the area of magnetic properties of materials. The intent

of this thesis was to improve the process of testing medical devices in a MR scanner bore, and it was able to lay the groundwork for those who wish to continue along this path.

5. References

1. Schenck, J.F., *Physical interactions of static magnetic fields with living tissues.* Progress in Biophysics and Molecular Biology, 2005. **87**(2–3): p. 185-204.

2. *MRI Bioeffects, Safety, and Patient Management*. 2014, Los Angeles, CA: Biomedical Research Publishing Group.

3. Woods, T.O., *Standards for medical devices in MRI: Present and Future.* Journal of Magnetic Resonance Imaging, 2007. **26**(5): p. 1186-1189.

4. ASTM, *Standard Test Method for Measurement of Magnetically Induced Displacement Force on Medical Devices in the Magnetic Resonance Environment*. 2015.

5. Brown, M.A. and R.C. Semelka, *MRI : Basic Principles and Applications*. Vol. 2nd ed. 1999, New York: John Wiley & Sons, Inc. [US].

6. *How do Gaussmeters work?: Hall Effect Theory - Gaussmeter Working Principle*. 2017; Available from: https://www.gaussmeter.co.uk/gaussmeter-working-principle.

7. Shellock, F.G., *Biomedical Implants and Devices: Assessment of Magnetic Field Interactions With a 3.0-Tesla MR System.* Journal of Magnetic Resonance Imaging 2002. **16**: p. 721-732.

8. *Lenz's Law*, in *A Dictionary of Physics*. 2009, Oxford University Press.

9. Rennie, J.L.a.R., ed. *A Dictionary of Physics*. 7 ed. 2015, Oxford University Press.

10. Abrahams, E.a.K., Frederic, *Diamagnetism.* 2014.

11. Abrahams, E.a.K., Frederic, *Paramagnetism.* 2014.

12. Abrahams, E.H., Jan F. ; and Keffer, Frederic. *Ferromagnetism*. 2014; Available from: http://www.accessscience.com/content/ferromagnetism/254600.

13. Abrahams, E.a.K., Frederic, *Magnetic susceptibility.* 2014.

14. Bleaney BI, B.B., *Electricity and Magnetism*. 2nd ed. 1965, Amen House, London: Oxford University Press.

15. *Steel 1010*, in *Saturation curves for soft magnetic materials*, F.P. LLC, Editor. 2017.

16. H.J. Qi, M.C.B., *Stress-Strain Behavior of Thermoplastic Polyurethane*, in *Department of Mechanical Engineering*. 2004, Massachusetts Institute of Technology: Cambridge, MA.

Appendix A

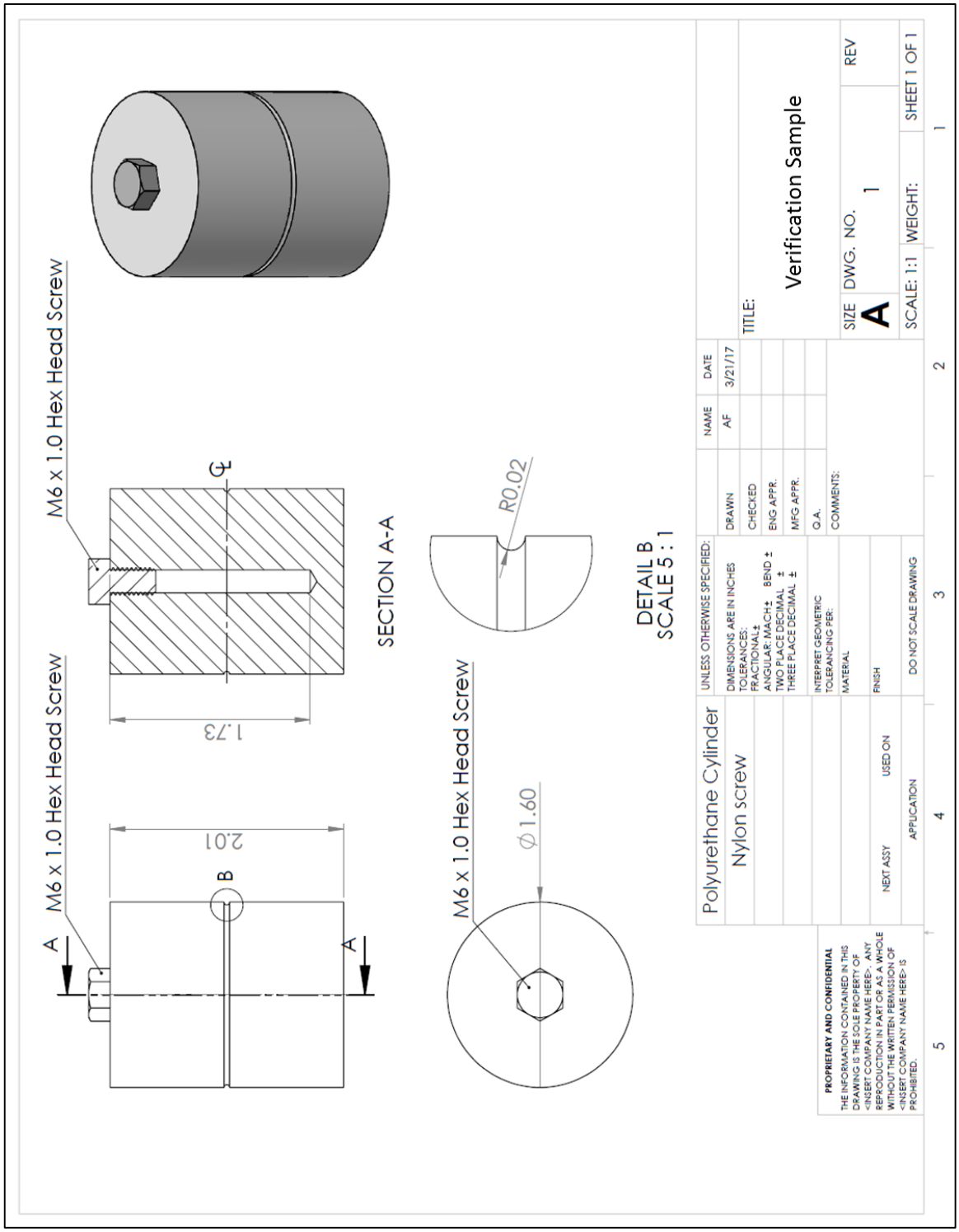
M6 x 1.0 Hex Head Screw
M6 x 1.0 Hex Head Screw
M6 x 1.0 Hex Head Screw
2.01
1.73
SECTION A-A
R0.02
Ø1.60
DETAIL B
SCALE 5 : 1
Polyurethane Cylinder
Nylon screw
UNLESS OTHERWISE SPECIFIED:
DIMENSIONS ARE IN INCHES
TOLERANCES:
FRACTIONAL ±
ANGULAR: MACH ± BEND ±
TWO PLACE DECIMAL ±
THREE PLACE DECIMAL ±
INTERPRET GEOMETRIC TOLERANCING PER:
MATERIAL
FINISH
DO NOT SCALE DRAWING
DRAWN
CHECKED
ENG APPR.
MFG APPR.
Q.A.
COMMENTS:
NAME
AF
DATE
3/21/17
TITLE:
Verification Sample
SIZE
A
DWG. NO.
1
REV
SCALE: 1:1
WEIGHT:
SHEET 1 OF 1
PROPRIETARY AND CONFIDENTIAL
THE INFORMATION CONTAINED IN THIS DRAWING IS THE SOLE PROPERTY OF <INSERT COMPANY NAME HERE>. ANY REPRODUCTION IN PART OR AS A WHOLE WITHOUT THE WRITTEN PERMISSION OF <INSERT COMPANY NAME HERE> IS PROHIBITED.
NEXT ASSY
USED ON
APPLICATION

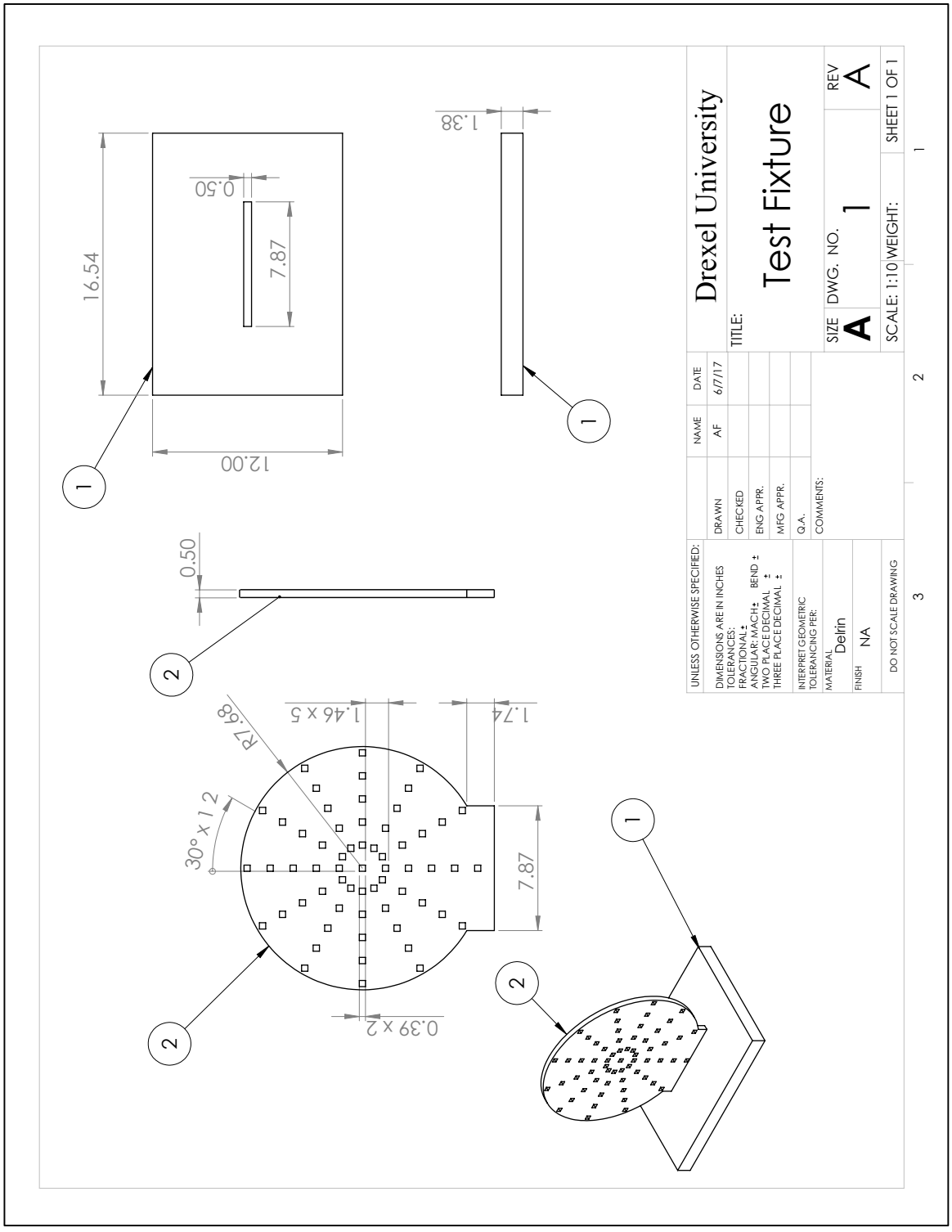
16.54
0.50
7.87
12.00
1.38
1
0.50
2
R7.87
1.46 x 5
1.74
30° x 12
7.87
0.39 x 2
2
1
2
UNLESS OTHERWISE SPECIFIED:
DIMENSIONS ARE IN INCHES
TOLERANCES:
FRACTIONAL ±
ANGULAR: MACH ± BEND ±
TWO PLACE DECIMAL ±
THREE PLACE DECIMAL ±
INTERPRET GEOMETRIC TOLERANCING PER:
MATERIAL Delrin
FINISH NA
DO NOT SCALE DRAWING
NAME DATE
DRAWN AF 6/7/17
CHECKED
ENG APPR.
MFG APPR.
Q.A.
COMMENTS:
Drexel University
TITLE:
Test Fixture
SIZE A
DWG. NO. 1
REV A
SCALE: 1:10 WEIGHT:
SHEET 1 OF 1
1
2
3

Appendix B

ANOVA Table

Source	SS	df	MS	F	Prob>F
Columns	306.154	2	153.077	2.84132e-06	1
Error	12283550782.095	228	53875222.728		
Total	12283551088.248	230			

Figure 22: ANOVA result table output from MATLAB.

Appendix C

Table 3: Average angular displacement of experimental test samples.

Number of Beads	Average Angular Displacement (degrees)	Standard Deviation
0	0.00	0.00
5	5.33	1.15
10	11.33	0.58
15	17.67	0.58
20	22.67	0.58
25	28.00	1.00
30	31.67	0.58
35	37.00	0.00
40	40.00	0.00
45	43.67	0.58
50	47.33	1.15
55	51.67	0.58
60	54.33	0.58
65	57.67	0.58
70	61.00	0.00
75	65.00	0.00
80	69.00	1.00
90	76.67	0.58
100	89.67	1.15

Table 4: Final results of the COMSOL simulation compared with the experimental data values. The simulation and experimental columns are measured in degrees.

Number of Beads	Simulation	Experimental	Relative Error (%)
0	0.00	0.00	0.00
5	2.66	5.33	50.06
10	6.14	11.33	45.85
15	10.43	17.67	40.94
20	16.14	22.67	28.78
25	23.57	28.00	15.79
30	27.33	31.67	4.47
35	32.51	37.00	11.55
40	37.70	40.00	18.64
45	42.88	43.67	21.15
50	48.06	47.33	20.22